View Article Online
View Journal

Journal of Materials Chemistry A

Accepted Manuscript

This article can be cited before page numbers have been issued, to do this please use: Y. Yang, P. Ying, J. Wang, X. Liu, Z. Du, Y. Chao and J. Cui, *J. Mater. Chem. A*, 2017, DOI: 10.1039/C7TA05253G.

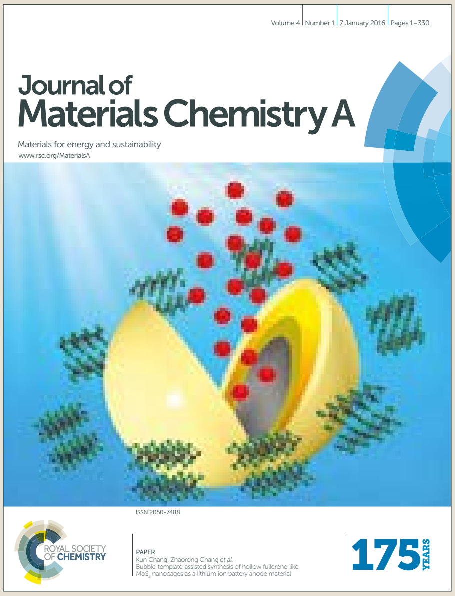

Volume 4 | Number 1 | 7 January 2016 | Pages 1–330

Journal of Materials Chemistry A

Materials for energy and sustainability

www.rsc.org/MaterialsA

ISSN 2050-7488

ROYAL SOCIETY OF CHEMISTRY

PAPER
Kun Chang, Zhaorong Chang et al.
Bubble-template-assisted synthesis of hollow fullerene-like MoS_2 nanocages as a lithium-ion battery anode material

175 YEARS

ROYAL SOCIETY OF CHEMISTRY

rsc.li/materials-a

View Article Online
DOI: 10.1039/C7TA05253G

Journal Name

RSCPublishing

ARTICLE

Cite this: DOI: 10.1039/x0xx00000x

Received 00th January 2017, Accepted 00th January 2017

DOI: 10.1039/x0xx00000x

www.rsc.org/

Enhancing thermoelectric performance of Cu_3SnS_4-based solid solutions through coordination of the Seebeck coefficient and carrier concentration

Yuanbo Yang,[a,b] Pengzhan Ying,[*a] Jinzhi Wang,[b] Xianglian Liu,[b] Zhengliang Du,[b] Yimin Chao,[*c] Jiaolin Cui[*b]

To improve the thermoelectric (TE) performance of Cu_3SnS_4 is challenging because it exhibits a metallic behavior, therefore, a strategy should be envisaged to coordinate the carrier concentration (n_H) and Seebeck coefficient (α). The coordination in this work has been realized through the Fermi level (E_f) unpinning and shifting towards the conduction band (CB) via an addition of excess Sn in Cu_3SnS_4. As a result, the solid solution $Cu_3Sn_{1+x}S_4$ (x=0.2) has the moderate α (178.0 μVK^{-1}) at 790 K and high n_H (1.54×10^{21} cm^{-3}) values. Along with the lowest lattice thermal conductivity κ_L (0.39 $WK^{-1}m^{-1}$) caused by the increased phonon scattering by carriers, the highest ZT value of 0.75 is attained at ~790 K. This value is 2.8 times that of the stoichiometric Cu_3SnS_4, and stands among the tops for the ternary Cu-Sn-S sulfide thermoelectrics at the corresponding temperatures. More importantly, this approach used in the ternary Cu_3SnS_4 provides a guidance or reference to improve the TE performance of other materials.

1. Introduction

Ternary chalcogenides Cu-Sn-S based compounds[1-3] or oxide ceramics[4,5] have attracted much attention in thermoelectrics in recent years, due to earth-abundance of constituent elements or thermal stability in air. Therefore, the development of these materials is crucial if thermoelectrics is to supply a significant fraction of the world's energy needs. In the Cu-Sn-S system, several ternary compounds have extensively been investigated as candidates for photovoltaic absorbers, including Cu_2SnS_3,[6,7] Cu_3SnS_4,[7,8] Cu_4SnS_4,[9,10] $Cu_2Sn_3S_7$,[10,11] etc. However, limited attention, to our knowledge, has been paid as TE candidates so far.[1-3] The reported ternary Cu-Sn-S TE families mostly are on $Cu_4Sn_7S_{16}$ (ZT~0.30 at 600 K,[1] and 0.41 at 863 K[12]), Zn(In)-doped Cu_2SnS_3 (ZT= ~0.58 at 723-773 K),[2,13] and a mixture of CuS and CuSn (ZT = 0.60 at 370-570 K).[14] Hence, it is urgent either to develop new Cu-Sn-S alternatives or significantly improve the TE performance of existing Cu-Sn-S ternary compounds.

The main drawback of restricting the applications of Cu-Sn-S compounds in thermoelectrics is their low electrical conductivities (σ) likely due to their wide bandgap (0.93-1.35 eV for Cu_2SnS_3,[6,7] 1.0~1.80 eV for Cu_3SnS_4[15-17] and 0.8 eV for $Cu_4Sn_7S_{16}$[3]), and inharmonious relation of the Seebeck coefficient (α) and carrier concentration (n_H). Hence it is challenging to significantly improve their TE performance, which is described by the dimensionless figure of merit (ZT), ZT=$T\alpha^2\sigma / \kappa = T\alpha^2\sigma / (\kappa_e+\kappa_L)$. Here T is the absolute temperature, and κ, κ_e and κ_L are the total, electronic and lattice thermal conductivity respectively.

Cu_3SnS_4 is a p-type semiconductor with the bandgap E_g ranging from 1.0 eV to 1.8 eV.[15-17] This compound is easy to be synthesized because it has a wide thermodynamic stability window due to a large chemical potential phase space.[18,19] However, differing from Cu_2SnS_3 that contains only two Cu(I) ions, the Cu_3SnS_4 compound formally contains two Cu(I) and one Cu(II) ions per formula unit. Since every formal Cu(II) ion creates one free hole,[18,19] the Cu_3SnS_4 is usually a degenerate p-type semiconductor with a high carrier concentration (~6×10^{21} cm^{-3})[18,19] and low electrical resistivity (3.5-7.4×10^{-4} Ω.cm).[15,20] In addition, it is also different from $Cu_4Sn_7S_{16}$ either as the compound $Cu_4Sn_7S_{16}$ reserves 1/4 unoccupied Cu sites in the crystal structure, which serve as a shallow acceptor-like defect.[1] In addition, $Cu_4Sn_7S_{16}$ is an n-type semiconductor.[1]

Owing to its inherent carrier concentration (~6×10^{21} cm^{-3}) higher than the optimal one (10^{19}~10^{21} cm^{-3}),[21] the compound Cu_3SnS_4 exceptionally exhibits the metallic behavior with low Seebeck coefficient, hence the pristine Cu_3SnS_4 is never a good TE candidate. In order to improve its TE performance, it is strongly suggested to harmonize the Seebeck coefficient and carrier concentration. This strategy is feasible as the unpinning of the Fermi level (E_f) via the movement of the E_f towards the conduction band minimum (CBM) enables the adjustment of

View Article Online
DOI: 10.1039/C7TA05255G

both the carrier concentration and local density of states (DOS) over a narrow energy range, leading to the increasing of the Seebeck coefficient.[22] While the unpinning of the E_f can be realized by the creation of the antisite defect Sn_{Cu} in Cu_3SnS_4, as the defect Sn_{Cu}, acting as a dopant, has deep states with the transition from +1 to +3 located 0.2 eV below the CBM, and is energetically favorable in Cu_3SnS_4.[19] Therefore, the band structure engineering via the creation of defect Sn_{Cu} species can coordinate the carrier concentration and Seebeck coefficient, then improve the TE performance.

2. Experimental

2.1 *Sample preparation*

The mixtures, consisting of three elements Cu, Sn and S according to the formula $Cu_3Sn_{1+x}S_4$ (x=0, 0.1, 0.2, 0.3), were loaded into four different vacuum silica tubes, and then heated to 723 K in 4.5 h followed by holding for 2 h. The subsequent heating from 723 K to 1223 K was carried out in ~7 h, and holding at 1223 K for ~3.5 h. Afterwards, the melted mixtures were cooled to 1073 K in 2 h with the holding time at this temperature for 48 h. Finally, the melts were cooled to room temperature (RT) in the furnace for the synthesis of the solid solutions. The ingots were subsequently ball milled for 5 h, prior to consolidation using spark plasma sintering (SPS) at the highest sintering temperature of 923 K and pressure of 60 MPa. The holding time at 923 K is about 2 min. The densities of the sintered samples were measured by using Archimedes' method. Each sample was cut into 3 mm slices measuring 2.5 × 12 mm^2 out of the sintered block with the size of ϕ 20 × 2.5 mm^2 for electrical property measurements. After polishing the surfaces of the two sides, coin-shaped blocks with the size of ϕ10 × 1.5 mm^2 were prepared for thermal diffusivity measurements.

2.2 *Physical property Measurements*

The electrical properties including Seebeck coefficient (α) and electrical conductivity (σ) were measured using a ULVAC ZEM-3 instrument system under a helium atmosphere from RT to ~800 K, with measurement uncertainties of ~5.0% for both of them. During the measurement of Seebeck coefficient, a temperature difference of around 5^{o}C was applied to the two terminals of each sample, while the measurement of the electrical conductivity was conducted using a four-probe method. The thermal diffusivities (λ) were measured by using TC-1200RH apparatus, with uncertainties of about 10%. The heat capacities (C_p) were estimated using the Dulong–Petit rule. The total thermal conductivities (κ) were determined according to the formulae $\kappa = dC_p\lambda$, here d is the material density. The three physical parameters (α, σ and κ) were finalized by measuring three times each. The total uncertainty of the ZT value is estimated as 18%.

The lattice contributions (κ_L) were calculated by subtracting the electronic contribution (κ_e) from the total κ, i.e., $\kappa_L = \kappa - \kappa_e$. Here κ_e is expressed by the Wiedemann–Franz law, $\kappa_e = L_0\sigma T$, where L_0 is the Lorenz number, estimated as 2.0×10^{-8} $W\Omega K^{-2}$ for the current semiconductors,[23] close to the value (~2.2×10^{-8} $W\Omega K^{-2}$) reported in *ref*.[24]. The Hall coefficient (R_H) measurements at RT were conducted with a Hall effect measurement system (PPMS, Model-9) using a four-probe configuration with a magnetic field sweeping between ±5.0 T. The rectangular samples with the size of 2×2×7 mm^3 were prepared for measurement. The Hall mobility (μ) and carrier concentration (n_H) were subsequently determined according to the relationships $\mu = |R_H|\sigma$ and $n_H = 1/(eR_H)$, respectively, where e is the electron charge.

2.3 *Chemical compositions and structural analyses*

The chemical compositions were determined using an electron probe micro-analyzer (EPMA) (S-4800, Hitachi, Japan) with an accuracy of >97%.

The powder X-ray diffraction patterns of the samples were analyzed using an X-ray powder diffractometer (XRD) (D8 Advance) operated at 50 kV and 40 mA. Cu Ka radiation (l = 0.15406 nm) and a scan rate of 4^{o} min^{-1} were used to record the patterns in the range of 10^{o} to 100^{o}. The lattice constants a and c were obtained from the refinement of the X-ray patterns using Jade software.

2.4 *Electronic structure calculations*

The electronic structures were calculated using spin-polarized density functional theory (DFT) with the generalized approximation (GGA) of Perdew–Burke–Ernzerhof (PBE)[25] implemented in the Vienna *ab* initio simulation package (VASP, version 5.2.12).[26,27] The DFT+U methodology with a value of U = 5.0 eV was used in this work.[28] The valence electronic states were expanded in the plane wave basis set, with the core–valence interaction represented using the scalar relativistic projector augmented wave (PAW)[29] approach and a cut-off of 400 eV.

In the real material system $Cu_3Sn_{1+x}S_4$, there are two incorporations of extra Sn in the crystal lattice, (1): Occupation in the Cu sites, and (2): In the interstitial sites. In the present calculations the arrangement of Sn is randomized, therefore the most stable structures are used for calculation. Considering the large cell volume and calculation burden, the density of states of $Cu_6Sn_{2+y}S_8$ (y=0,1,2) (Sn is in the interstitial sites) and $Cu_{24-y}Sn_{8+y}S_{32}$ (y=0,1,2,3,4) (Sn occupying Cu sites) have been calculated using HSE06 functional with a more accurate single point electronic structure calculation. The detailed arrangements of Sn in the unit cell are described in the section *3.3*.

3. Results and discussions

3.1 *XRD and composition analyses*

Fig.S1 is the EMPA mappings (Fig.S1a-c) of three elements Cu, S and Sn along with the energy dispersive spectrum (EDS) (Fig.S1d) for the sample at x=0.2. The chemical compositions of stoichiometric Cu_3SnS_4 and $Cu_3Sn_{1.2}S_4$ are shown in Table S1, where the number of S moles is normalized to 4. Generally, the three elements are distributed uniformly in the matrix without much segregation observed. The relative molar fractions shown in

View Article Online
DOI: 10.1039/C7TA05253G

Table S1 are close to those of the nominal ones, except for a slight excess in Cu and Sn, which might be resulted from the evaporation of S during the material processing.

The XRD patterns of the powders are presented in Fig.1a, where a single Cu_3SnS_4 phase has been identified at $x≤0.2$ with tetragonal structure (space group: I-42m) (PDF: 330501), in agreement with the result reported in *ref.* [7], instead of the orthorhombic one (Pmn21).[15,16] At $x=0.3$ trace impurity phase Sn_2S_3 (PDF:14-0619) is visible, indicating that the solubility of excess Sn (x value) in ternary $Cu_3Sn_{1+x}S_4$ is less than 0.3. Look at the main peaks in the regions of 26°-34° and 40°-60°, one can see these peaks shift toward low diffraction angles with Sn content increasing (see Fig.1b). This suggests that the lattice structure suffers dilation. In other hand, the lattice constants a and c increases linearly with x value increasing, and follow the Vegard's law, as shown in Fig.1c, indicating that the excess Sn has already incorporated into the crystal lattice. The a and c values for the pristine Cu_3SnS_4 are 5.40 and 10.83 Å respectively.

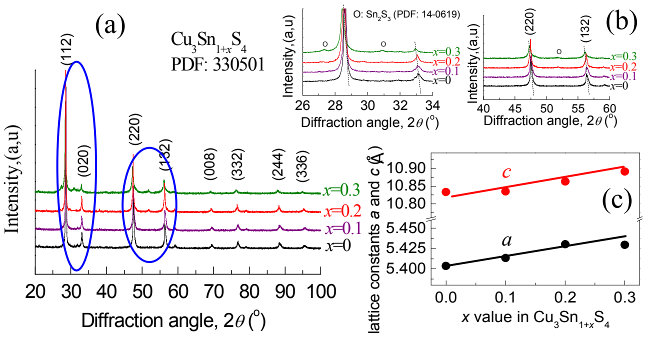

Fig.1 (a) X-ray diffraction patterns of $Cu_3Sn_{1+x}S_4$ (x=0, 0.1, 0.2, 0.3) powders; (b) Two close-up views with the 2θ ranging between 26°-34°, and 40°-60°; (c) Lattice constants a and c, which increase with x value increasing, follow the Vegard's law.

3.2 Microstructure observations

In order to further confirm the synthesis of Cu_3SnS_4-based ternary compounds, the microstructures have been examined by using high resolution TEM (HRTEM) for the samples at x=0 and 0.2, shown in Fig.2 and 3. Fig.2a is the TEM image of the sample with x=0, and Fig.2b is the corresponding HRTEM image. The inset in Fig.2b is its magnified image, showing the d spacing between (112) crystal planes is about 0.31 nm. Fig.2c is its corresponding selected area electron diffraction (SAED) pattern and Fig.2d is showing the EDS measurement results. These observations confirm the structure of the synthesized Cu_3SnS_4 solid solution.

Fig.3a,b are the TEM image and its corresponding SAED pattern for the sample at x=0.2. Fig.3c is the HRTEM image and Fig.3d is an enlarged image, which shows that the d spacing between (220) crystal planes is ~0.20 nm. This spacing is in good agreement with that in the XRD pattern.

3.3 First principle calculations

Since the excess Sn is incorporated into the Cu_3SnS_4 crystal lattice, the band structure should be modified. To better understand the band structure alterations, we have calculated the density of states (DOS) and formation energies (d_H) of $Cu_6Sn_{2+y}S_8$ (y=0,1,2) and $Cu_{24-y}Sn_{8+y}S_{32}$ (y=0,1,2,3,4). The results are shown in Fig.4 and 5. The panel A in Fig.4, arranging in sequence from y=0 to y=2 from left to right, represents the crystal structures upon different Sn incorporations into the interstitial sites, and the blue balls circled using wine color represent incorporated Sn atoms. The panel B is the DOS of different materials, where the Fermi level (E_f) unpins and gradually moves toward the conduction band (CB) with

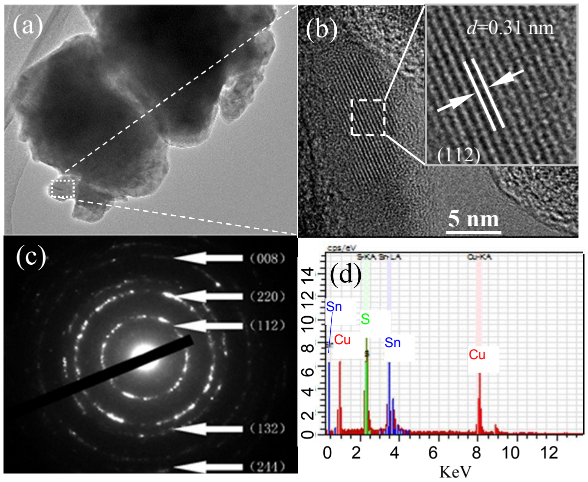

Fig.2 High resolution transmission electron microscopy (HRTEM) image observed in Cu_3SnS_4. (a) TEM image; (b) The corresponding high resolution TEM image, the inset is the magnified high resolution TEM image, which shows that the spacing between (112) crystal planes is about 0.31 nm. (c) The selected area electron diffraction (SAED) pattern; (d) Chemical compositions analyses.

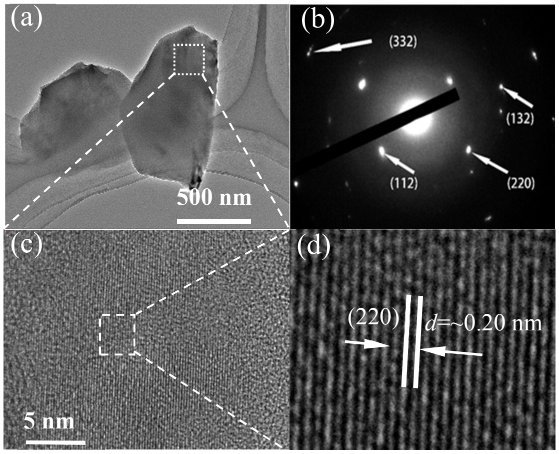

Fig.3 High resolution transmission electron microscopy (HRTEM) image observed in $Cu_3Sn_{1.2}S_4$. (a) TEM image; (b) The selected area electron diffraction (SAED) pattern; (c) The corresponding high resolution TEM image; (d) Magnified high resolution TEM image, which shows that the spacing between (220) crystal planes is about ~0.20 nm.

View Article Online
DOI: 10.1039/C7TA05253G

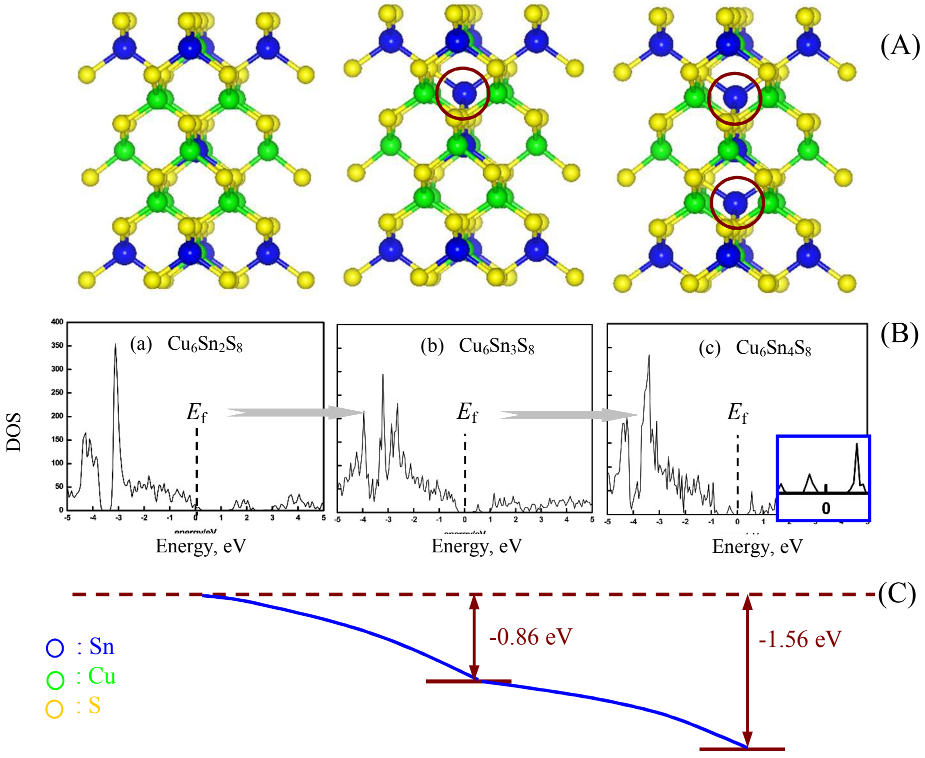

Fig. 4. The results from the first principle calculation. (a) Panel A, arranging in sequence from y=0 to y=2 from left to right, presents the tetragonal structures with different arrangements of Sn in the interstitial sites in $Cu_6Sn_{2+y}S_8$ (y=0,1,2). The enclosed balls represent incorporated Sn atoms into the interstitial sites; (b) Panel B are the density of States (DOS) for different Sn incorporations, indicating that the Fermi level (E_f) unpins and moves towards the conduction band. However, the deep impurity levels creates near the middle of the bandgap (an inset in panel B(c) is the close-up view of the impurity levels labeled by blue lines); (c) Panel C is the overall total-formation energy (d_H) profile when the different Sn is incorporated.

Sn content increasing, although the calculated bandgap (E_g) (E_g = ~1.25 eV) remains almost constant. The calculated E_g values are lower than those reported (1.5~1.6 eV),[17] which might be due to the GGA problem.[30,31] However, the impurity levels gradually creates within the gap as y value increases, see the magnified pattern as an inset in panel B(c), and this level seems to merge with the conduction band with Sn content increasing. The panel C in Fig.4 is the formation energy (d_H) profile with different Sn incorporations, which reduces from 0 to -1.56 eV at y=2. These results suggest that Sn is energetically favorable to the interstitial site when Sn is in excess, which unpins the Fermi level and allows the E_f to shift toward the conduction band. Besides, the impurity levels become more obvious within the gap with Sn content increasing, see Fig.4B (c).

The results for $Cu_{24-y}Sn_{8+y}S_{32}$ (y=0,1,2,3,4) from the first principle calculation are shown in Fig.5. Similarly, the Fermi level (E_f) unpins and gradually moves toward the conduction band (CB) with Sn content increasing. The negative formation energies (d_H) suggest that Sn is energetically favorable to the Cu sites either. The above results indicate that the extra Sn in current materials, whether it occupies the interstitial or Cu sites, is inclined to stabilize the structure, creating the defect species Sn_i, or Sn_{Cu}^{3+} and Sn_{Cu}^{2+}. However, it still remains a challenge to figure out how much defect Sn_i or Sn_{Cu}^{3+} and Sn_{Cu}^{2+} in the defect clusters in the synthesized samples. These calculations are beyond the current limit of the investigations. Besides, the Sn content incorporated into the lattices should be limited due to limited solubility, that is why we have observed the increased formation energy at y=4.

View Article Online
DOI: 10.1039/C7TA05253G

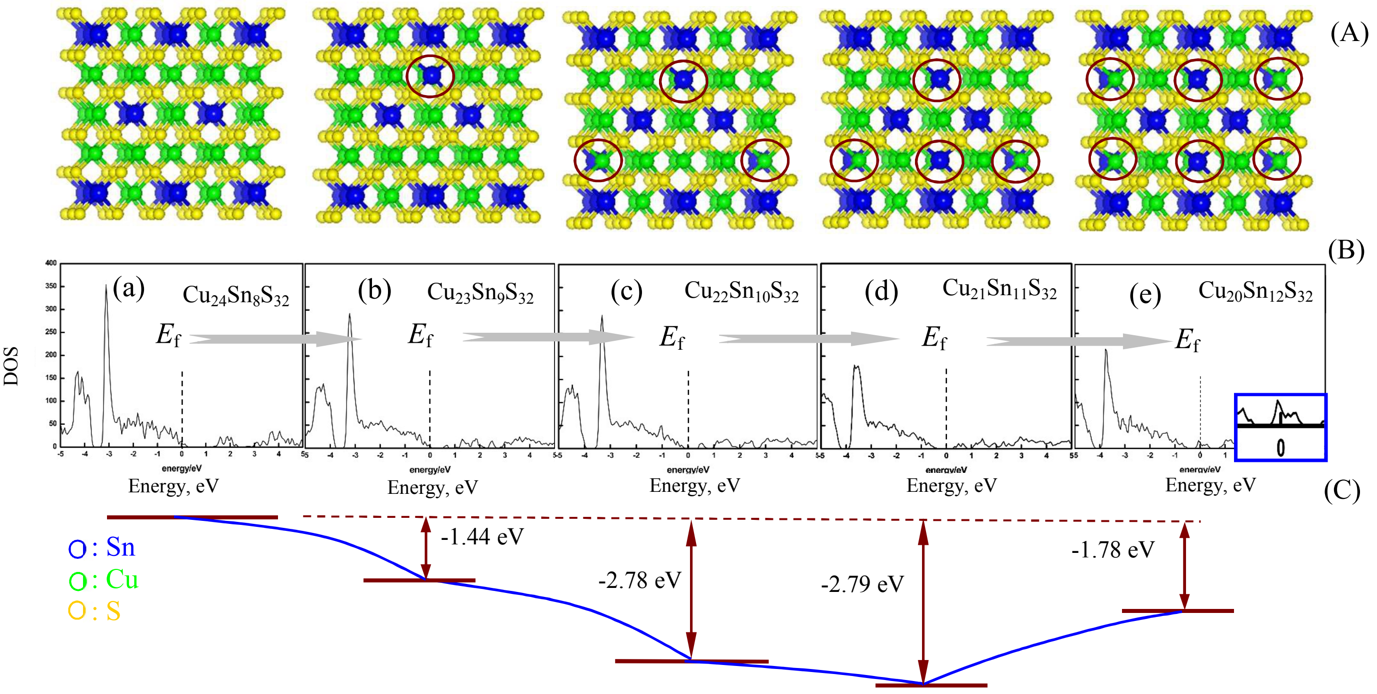

Fig. 5. The results from the first principle calculation. (a) Panel A, arranging in sequence from y=0 to y=4 from left to right, presents the tetragonal structures with different arrangements of Sn in the Cu sites in $Cu_{24-y}Sn_{8+y}S_{32}$ (y=0,1,2,3,4). The enclosed balls represent incorporated Sn atoms into the Cu sites; (b) Panel B are the density of States (DOS) for different Sn incorporations, indicating that the Fermi level (E_f) unpins and moves towards the conduction band. However, the deep impurity levels creates near the middle of the bandgap (an inset in panel B(e) is the close-up view of the impurity levels labeled by blue lines); (c) Panel C is the overall total-formation energy (d_H) profile when the different Sn is incorporated.

3.4 Transport properties

In order to better understand the effects of band structure engineering on the transport properties, we have specially measured the Hall coefficients (R_H) of $Cu_3Sn_{1+x}S_4$ (x=0, 0.1, 0.2, 0.3) at RT, and then attained the Hall carrier concentrations (n_H) and mobility (μ). The results are shown in Fig.6. We observed that n_H value at x=0 is 4.25×10^{21} cm^{-3}, and that at x=0.3 is 4.27×10^{18} cm^{-3}, reducing by 3 orders of magnitude. While the mobility (μ) increases from 13.47 $cm^2V^{-1}s^{-1}$ (x=0) to 94.79 $cm^2V^{-1}s^{-1}$ (x=0.3) with Sn content increasing. Although the creation of the defect species Sn_i, Sn_{Cu}^{3+} or Sn_{Cu}^{2+} neutralizes the p-type holes to some extent, we believe that the significantly decreased n_H value with Sn content increasing is mainly due to the unpinning of the Fermi level, followed by its movement toward the conduction band. Besides, the associated impurity levels, acting as an annihilation center for electrons and holes, plays a role in reducing the n_H value. The precipitated Sn_2S_3 at x=0.3 identified using XRD, which is a n-type semiconductor,[32] might have a negative effect on the carrier concentration, however, we do not know its correlation with the impurity level yet.

3.5 TE performance

The reduction in n_H should have a profound impact on the TE performance, which was summarized in Fig.7. Fig.7a presents the positive Seebeck coefficients (α), indicating p-type semiconducting behavior of the materials. In addition, the α value increases with the measuring temperature increasing for all the samples, indicating the extrinsic conducting behavior. With Sn content increasing from x=0 to 0.3, the α value increases from 103.0 μVK^{-1} to 504.0 μVK^{-1} at ~790 K, while the electrical conductivity (σ) decreases from 1.3×10^5 $\Omega^{-1}cm^{-1}$ to 2.9×10^2 $\Omega^{-1}cm^{-1}$, as shown in Fig.7b, decreasing by ~3 orders of magnitude. At x=0.2 and 790 K the electrical conductivity is 2.0×10^4 $\Omega^{-1}cm^{-1}$.

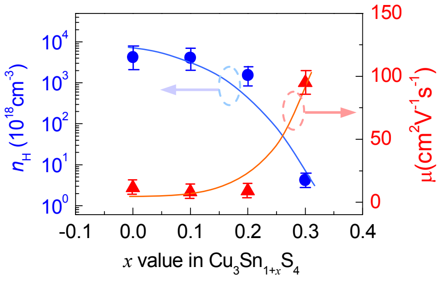

Fig.6 Measured Hall carrier concentration (n_H) and Mobility (μ) against x value in $Cu_3Sn_{1+x}S_4$.

View Article Online
DOI: 10.1039/C7TA05255G

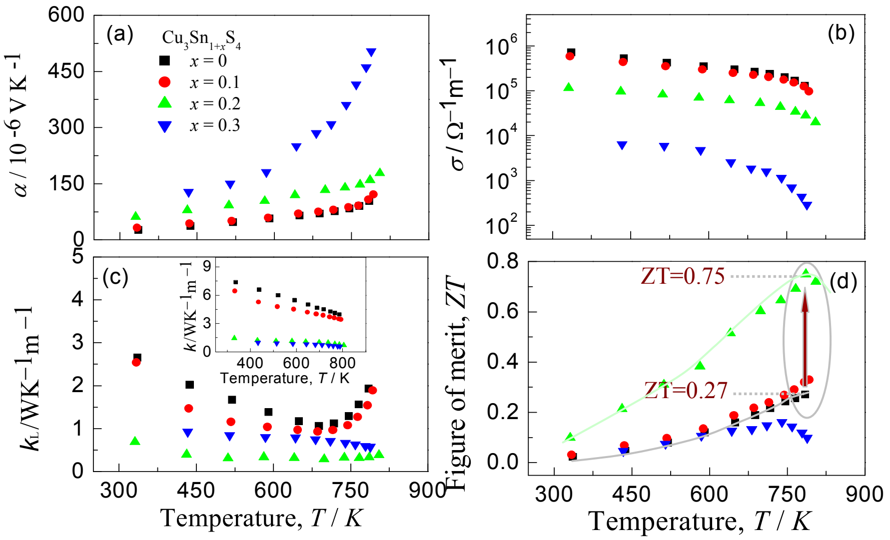

Fig.7 TE properties as a function of temperature, (a) Seebeck coefficient (α); (b) Electrical conductivity (σ); (c) lattice thermal conductivity (κ_L), the inset is the total κ; (d) ZT values.

The lattice thermal conductivity (κ_L), shown in Fig.7c, reduces from 1.93 $WK^{-1}m^{-1}$ (x=0) to 0.39 $WK^{-1}m^{-1}$ at ~790 K as Sn content increases to x=0.2, and above x>0.2 the sample gives the enhanced κ_L value (0.57 $WK^{-1}m^{-1}$). This might be due to the reduced scattering of phonons by carriers, because the n_H value at x=0.3 is rather lower than those at x=0.2. However, the temperature dependence of κ_L for the samples at x=0 and 0.1 is quite abnormal. The κ_L values for these two samples increase rapidly with temperature increasing above ~700 K, whereas the total thermal conductivities (κ) reduce linearly with temperature increasing, see the inset in Fig.7c. The abnormally increased κ_L values were confirmed by repeated measurements, and might involve the contribution of peripheral phonons,[33-34] which increases with the measuring temperature increasing, especially, when the donor levels merge with the conduction band[33,34] (see Fig.4 and 5), although the contribution of peripheral phonons is usually realized at the very low temperatures.[33,34] Alternatively, the enhanced κ_L values at high temperatures might also involve the contribution of photon conduction, κ_p, described below,[35]

$$\kappa_p = 16/3\ \sigma r^2 T^3 l_R \qquad (1)$$

here r is the refractive index in the medium, l_R the mean free path of photons. Based on the equation (1), the κ_p value is proportional to T^3. However, the photon conduction may usually be observed in some polycrystalline oxides, such as BaO and SrO,[36] Al_2O_3 and BeO,[37] and in single crystals of Al_2O_3, MgO, CaF_2 and TiO_2.[38] Therefore, the abnormally increased κ_L values at high temperatures requires further investigations.

Combined with the above three physical parameters, we have attained the TE figure of merit (ZT), as shown in Fig.7d. Because of high electrical and low thermal conductivities at x=0.2, the highest ZT value is 0.75 at ~790 K, while that at x=0 is only 0.27. Although this ZT value is still lower than those of state-of-the-art mid temperature TE materials, like elemental tellurium (ZT=~1.0 at 700 K),[39] PbTe- (ZT=2.5 at 923 K)[40] and SnSe-based (ZT=1.7 at 873 K) alloys,[41,42] it stands among the tops for ternary Cu-Sn-S sulfides at the corresponding temperatures.

The increasing of a and c values indicate the expansion of the unit cell, which has a potential to modify the band structure and improve the TE performance, as those indicated in the CoSbS surfide.[43] In order to better understand the band structure alterations, we present the Pisarenko plots[21] in Fig.8a, assuming m^* = 0.2, 3.5, and 4.5 m_e at RT, in which the measured Seebeck coefficients (α) for the Sn-incorporated samples (labeled by ★ symbol) are roughly between the lines with m^* =3.5 m_e and 4.5 m_e, decreasing slightly with increasing n_H. However, if we carefully fit the measured α values as a function of carrier concentration n_H, a $\alpha \sim n_H^{-1/3}$ dependence is obtained, instead of the Pisarenko relationship ($\alpha \sim n_H^{-2/3}$). This suggests that the $\alpha \sim n_H$ relation does not exactly follow the single parabolic model (SPB). Although there are many defects in $Cu_3Sn_{1+x}S_4$, such as Sn_i, Sn_{Cu}, Cu_i (Cu in the interstitial sites), and possibly created p-type compensating defects Cu_{Sn}, V_{Sn} and V_{Cu}, only Sn_{Cu} is energetically favorable in the Cu-Sn-S material system.[19] This implies that the compensating defects (Cu_{Sn}, V_{Sn} and V_{Cu}) in the current materials should have little impact on the Fermi level (E_f)

View Article Online
DOI: 10.1039/C7TA05253G

unpinning (Fig.5b). It is the preferential occupation of Sn in the interstitial or Cu sites that engineers the band structure, and then reduces the n_H value significantly. Besides, the extra electrons provided by the dopants ${Sn_{Cu}}^{2+}$ or ${Sn_{Cu}}^{3+}$ themselves have a limited contribution in reducing n_H either. This conclusion is not in agreement with that reported by Fan etc.,[44] who suggests that in the Ga and In co-doped Cu_2SnSe_3 system the defects have a dominant effect on the carrier concentration.[44]

In order to confirm our hypothesis, we have calculated the carrier density in Sn-incorporated Cu_3SnS_4 environment using the valence counting rule,[45-47] based on the following descriptions without taking into account the creation of the compensating defects,

$$n_{cal.}=(1-3x/8)n_{H0}, \quad \text{for } {Sn_{Cu}}^{3+} \text{ species} \qquad (2)$$

$$\text{or,} \quad n_{cal.}=(1-2x/8)n_{H0} \quad \text{for } {Sn_{Cu}}^{2+} \text{ species} \qquad (3)$$

Here n_{H0} is the experimentally measured Hall carrier concentration for the pristine Cu_3SnS_4, $n_{H0}=4.25\times10^{27}$ m^{-3}. The calculated results are presented in Fig.8b. It is apparent that there is no agreement between the measured Hall carrier concentrations n_H and the calculated $n_{cal.}$ values. The theoretically calculated $n_{cal.}$ values are almost unchanged. If the compensating defects with an opposite charge are taken into account, the estimated $n_{cal.}$ values should be a little higher than those from the equation (2) and (3). But it is obvious that such estimations could not change the tendency described in Fig.8(b). The slightly decreased α value with carrier concentration increasing, as shown in Fig.8a, suggests that the coordination between the carrier concentration and Seebeck coefficient has been realized in the current $Cu_3Sn_{1+x}S_4$ solid solutions. Besides, owing to the reduction in n_H with Sn content increasing, the mobility μ increases, as shown in Fig.6, caused by the increasing of the carrier scattering time (τ), according to the equation (4):

$$\mu = e\tau / m^* \qquad (4)$$

here e is the electron charge.

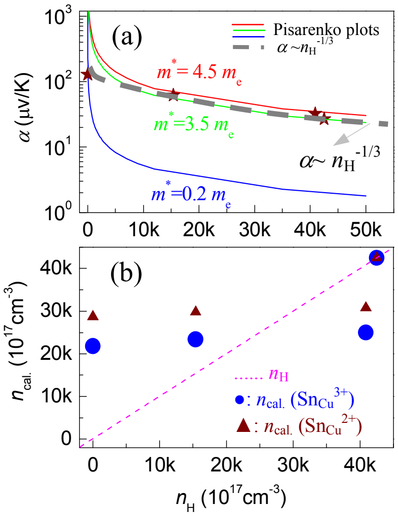

Fig.8 (a) The Pisarenko plots assuming the effective mass m^* = 0.2, 3.5, 4.5 m_e and T = 295 K. The data labeled by '★represents the α values in this work at determined n_H values, which follow the $\alpha\sim n_H^{-1/3}$ relationship; (b) Calculated carrier concentrations ($n_{cal.}$). The symbols "●" and "▲" represent the n_{cal} values upon the creation of ${Sn_{Cu}}^{3+}$ and ${Sn_{Cu}}^{2+}$ respectively.

Since at x=0.2 the ternary $Cu_3Sn_{1.2}S_4$ compound has the lowest lattice contribution (κ_L) and relatively high effective mass m^*, therefore, we estimate that it has a high quality factor B, according to the following relation,[23]

$$B = \mu(m^*/m_e)^{3/2}T^{5/2}/\kappa_L \qquad (5)$$

The detailed B value is plotted in Fig.9, in which the effective mass m^*/ m_e is also shown. As x value increases both the m^*/ m_e and B values increase up to x=0.2, then rapidly decrease. These results further confirms that x=0.2 is a critical Sn content in $Cu_3Sn_{1+x}S_4$ at which the highest TE performance can be expected.

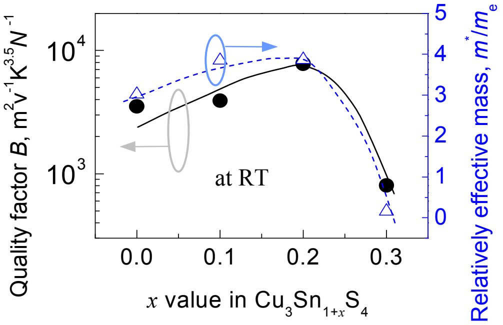

Fig. 9 The relatively effective mass (m^*/m_e) (Δ) and quality factor B (●) at RT, defined by $B = \mu (m^*/m_e)^{3/2}T^{5/2}/\kappa_L$, as a function of x. At x = 0.2 both the effective mass m^*/m_e and quality factor B value reach the highest.

4. Conclusions

Ternary $Cu_3Sn_{1+x}S_4$ solid solutions with an excess of Sn have been synthesized and their thermoelectric properties have been examined. The first principle calculations reveal that the Fermi level (E_f) unpins and moves towards the conduction band (CB) with Sn content (x value) increasing, which effectively harmonizes the Seebeck coefficient and carrier concentration. Combined with the lowest lattice thermal conductivity κ_L (0.39 $WK^{-1}m^{-1}$ at 790 K) at x=0.2 caused by the increased phonon scattering for carriers, a significant improvement in TE performance has been achieved with the ZT value of 0.75 at 790 K, about 2.8 times that of the stoichiometric Cu_3SnS_4. This value stands among the highest in the ternary sulfide thermoelectric materials.

Conflicts of interest

There are no conflicts of interest to declare.

Acknowledgements

View Article Online
DOI: 10.1039/C7TA05253G

This work is supported by the National Natural Science Foundation of China (51671109, 51171084), and Zhejiang Provincial Natural Science Foundation (LY14E010003,LQ14E010001). We are also grateful for the first principles calculations from Prof. Y.Gao and Dr. Z.K.Han (Shanghai Institute of Applied Physics, Chinese Academy of Sciences).

Notes and references

1 C. Bourgès, P. Lemoine, O. I. Lebedev, R. Daou, V. Hardy, B. Malaman and E. Guilmeau, *Acta Mater*., 2015, **97**, 180.

2 Y. Shen, C. Li, R. Huang, R. Tian, Y. Ye, L. Pan, K. Koumoto, R. Zhang, C. Wan and Y. Wang, *Sci. Rep.*, 2015, **6**, 32501.

3 J. P. F. Jemetio, P. Zhou and H. Kleinke, *J. Alloys Compds*., 2006, **417**, 55.

4 Y. Liu , Y. Lin, Z. Shi, C.-W. Nan and Z. Shen, *J. Am. Ceram. Soc.*, 2005, **88**, 1337.

5 J. Lan , Y. Liu, B. Zhan, Y. Lin, B. Zhang, X. Yuan, W. Zhang, W. Xu and C.-W. Nan, *Adv. Mater*., 2013, **25**, 5086.

6 A. Crovetto, R. Chen, R. B. Ettlinger, A. C. Cazzaniga, J. Schou, C. Persson and O. Hansen, *Solar Energy Mater. Solar Cells*, 2016, **154**, 121.

7 H. Guan, H. Shen, C. Gao and X. He, *J. Mater. Sci: Mater. Electron*, 2013, **24**, 1490.

8 V. M. Dzhagan, A. P. Litvinchuk, M. Kruszynska, J. K.-Olesiak, M. Y. Valakh and D. R. T. Zahn, *J. Phys. Chem. C*, 2014, **118**, 27554.

9 H. Guan, H. Shen, C. Gao and X. He, *J. Mater. Sci: Mater. Electron*, 2013, **24**, 3195.

10 S. Fiechter, M. Martinez, G. Schmidt, W. Henrion and Y. Tomm, *J. Phys. Chem. Solids*, 2003, **64**, 1859.

11 T. Lui, F. Hung, T. Lui and K. Chen, *J. Nanomater*., 2015, **2015**, 969783 (1-7).

12 T. He, N. Lin, Z. Du, Y. Chao and J. Cui, *J. Mater. Chem. C*, 2017, **5**, 4206.

13 Q. Tan, W. Sun, Z. Li and J. F. Li, *J. Alloys Compds.*, 2016, **672**, 558.

14 M. Hasaka, T. Aki, T. Morimura and S.I. Kondo, *Energy Convers. Mgmt.*, 1997, **38**, 855.

15 U. Chalapathi, Y.B. K. Kumar, S. Uthanna and V. S. Raja, *AIP Conf. Proc*., 2012, **1447**, 649.

16 P. A. Fernandes, P. M. P. Salomé and A. F. da Cunha, *Phys. Status Solidi C*, 2010, **7**, 901.

17 Z. Su, K. Sun, Z. Han, F. Liu, Y. Lai, J. Li and Y. Liu, *J. Mater.Chem*., 2012, **22**, 16346.

18 P. Zawadzki, L. Baranowski, H. Peng, E. S. Toberer, D. S. Ginley, W. Tumas, A. Zakutayev and S. Lany, *Appl. Phys. Lett*., 2013, **103**, 253902.

19 L. L. Baranowski, P. Zawadzki, S. Christensen, D. Nordlund, S. Lany, A. C. Tamboli, L. Gedvilas, D. S. Ginley, W. Tumas, E. S. Toberer and A. Zakutayev, *Chem. Mater*., 2014, **26**, 4951.

20 P. A. Fernandes, *J. Phys. D: Appl. Phys*., 2010, **43**, 215403.

21 G. J. Snyder and E. S. Toberer, *Nat. Mater*., 2008, **7**, 105.

22 J. P. Heremans, V. Jovovic, E. S. Toberer, A. Saramat, K. Kurosaki, A. Charoenphakdee, S. Yamanaka and G. J. Snyder, *Science*, 2008, **321**, 554.

23 X. Shi, L. Chen and C. Uher, *Int. Mater. Rev*., 2016, **61**, 379.

24 K. C. Lukas, W. S. Liu, G. Joshi, M. Zebarjadi, M. S. Dresselhaus, Z. F. Ren, G.Chen and C. P. Opeil, *Phys. Rev. B: Condens. Matter Mater. Phys*., 2012, **85**, 205410.

25 J. Perdew, P. K. Burke and M. Ernzerhof, *Phys. Rev. Lett*.,1996, **77**, 3865.

26 G. Kresse and J. Furthmuller, *Phys. Rev. B: Condens. Matter Mater. Phys*., 1996, **54**, 11169.

27 G. Kresse and J. Furthmuller, *Comput. Mater. Sci*., 1996, **6**, 15.

28 M. Nolan, S. C. Parker and G. W. Watson, *Surf. Sci*., 2005, **595**, 223.

29 P. E. Blöchl, *Phys. Rev. B: Condens. Matter Mater. Phys*., 1994, **50**, 17953.

30 J. Cui, Y. Li, Z. Du, Q. Meng and H. Zhou, *J. Mater. Chem. A*, 2013, **1**, 677.

31 M. Han, K. Hoang, H. Kong, R. Pcionek, C. Uher, K. M. Paraskevopoulos, S. D. Mahanti and M. G. Kanatzidis, *Chem. Mater*., 2008, **20**, 3512.

32 A. Mary Saroja, I. Kartharinal Punithavathy, S. Johnson Jeyakumar, S. Joshua Gnanamuthu and A.R. Balu, *Optik*, 2017, **130**, 245.

33 K. S. Dubey and G. S.Verma, *Phys. Rev. B* 1971, **4**, 2071.

34 Z. K. Badir Khan and K. S. Dubey, *Solid State Commun*. 1981, **38**, 279.

35 D. W. Lee, and W. D. Kingery, *J. Am. Ceram. Soc*. 1960, **43**, 594.

36 A. E. Pengelly, *Brit. J. Appl. Phys*. 1995, **6**, 18.

37 M. McQuarrie, *J. Am. Ceram. Soc*. 1995, **37** [2, Part II], 91.

View Article Online
DOI: 10.1039/C7TA05253G

38 F. R. Charvat and W. D. Kingery, *J. Am. Ceram. Soc*. 1957, **40**, 306.

39 S. Lin, W. Li, Z. Chen, J. Shen, B. Ge and Y. Pei, *Nat. Commun*., 2016, **7**, 10287.

40 G. Tan, F. Shi, S. Hao, L. Zhao, H. Chi, X. Zhang, C. Uher, C. Wolverton, V. P. Dravid and M. G. Kanatzidis, *Nat. Commun.*, 2016, **7**, 12167.

41 G. Tang, W. Wei, J. Zhang, Y. Li, X. Wang, G. Xu, C. Chang, Z. Wang, Y. Du and L. Zhao, *J. Am. Chem. Soc*., 2016, **138**, 13647.

42 L. Zhao, G. Tan, S. Hao, J. He, Y. Pei, H. Chi, H. Wang, S. Gong, H. Xu, V. P. Dravid, C. Uher, G. J. Snyder, C. Wolverton and M. G. Kanatzidis, *Science*, 2016, **351**, 141.

43 S. Bhattacharya, R. Chmielowski, G. Dennler and G. K. H. Madsen, *J. Mater. Chem. A*, 2016, **4**, 11086.

44 J. Fan, H. Liu, X. Shi, S. Bai, X. Shi and L. Chen, *Acta Mater.*, 2013, **61**, 4297.

45 E. S. Toberer, A. F. May and G. J. Snyder, *Chem. Mater*., 2010, **22**, 624.

46 A. F.May, J. P. Fleurial and G. J. Snyder, *Chem. Mater*., 2010, **22**, 2995.

47 S. R. Brown, E. S. Toberer, T. Ikeda, C. A. Cox, F. Gascoin, S. M. Kauzlarich and G. J. Snyder, *Chem. Mater*., 2008, **20**, 3412.

[a] *Materials Science and Engineering College, China University of Mining and Technology, Xuzhou 221116, China*
**E-mail:* ypz3889@sina.com
[b] *School of Materials & Chemical Engineering, Ningbo University of Technology, Ningbo 315016, China*
**E-mail: cuijiaolin@163.com*
[c] *School of Chemistry, University of East Anglia, Norwich NR4 7TJ, United Kingdom. *E-mail: y.chao@uea.ac.uk*

Electronic Supplementary Information (ESI) available. See DOI: 10.1039/b000000x/

Table of Contents/Abstract Graphic

View Article Online
DOI: 10.1039/C7TA05253G